The International Journal of Advanced Manufacturing Technology
https://doi.org/10.1007/s00170-023-12618-0

ORIGINAL ARTICLE

Modeling and optimization of height-related geometrical parameters for thin wall structures manufactured by metal additive manufacturing

M. Rahmani Dehaghani[1] · Yifan Tang[1] · Suraj Panicker[2] · Di Wu[2] · Eric Coatanea[2] · G. Gary Wang[1]

Received: 27 July 2023 / Accepted: 26 October 2023

Abstract
Cold metal transfer wire arc additive manufacturing (CMT-WAAM) has attracted attention in recent years due to its ability to print walls with higher dimensional accuracy than regular WAAM. To print near-net shape parts by CMT-WAAM, there is a need to define a set of height-related geometrical parameters (HGPs) that can capture, quantify, and compare the quality of the height of the produced parts. In the presenting study, a set of HGPs, namely, the average height error, maximum height variation, and average absolute slope are defined and assessed. Fifteen single-track multi-layer walls are printed to check the effect of process parameters on the defined HGPs. It is found that the stability and quality of the print cannot be guaranteed by checking the visual appearance of the single beads and at least five-to-ten-layer walls should be printed. It is also found that the travel speed and the wire feed speed have positive monotonic relationships with average absolute slope and maximum height variation, respectively. Correlations between process parameters and HGPs are modeled and optimized using multi-objective optimization, and a validation test is performed to check the validity of the developed models. Moreover, HGPs of walls printed using unidirectional and bidirectional path strategies are calculated and compared. Defined HGPs are able to quantify, capture, and compare the quality of height of a wall with only three parameters. The HGPs can be used in further studies to report and compare the quality of height of thin wall structures.

Keywords Cold metal transfer · Wire arc additive manufacturing · Geometrical deviation · Multi-objective optimization

1 Introduction

Wire arc additive manufacturing (WAAM) is one of the directed energy deposition (DED) techniques that can produce large-scale metallic parts [1]. Compared to other metal additive manufacturing (AM) techniques, WAAM provides a higher material deposition rate which is favorable as it reduces the production time, but it suffers from dimensional inaccuracy, which limits its applications [2].

From the material point of view, WAAM can print materials with low weldability such as aluminum and low steel alloys [3, 4] especially when it is combined with the cold metal transfer (CMT) mode developed by Fronius. In CMT, the material deposition during welding happens in two steps. First, the welding torch generates an arc between the welding wire and the surface where the weld needs to be deposited. Second, the welding system detects a short-circuit in the arc and in turn retracts the wire, stopping the arc. Hence, CMT allows the molten metal droplet to transfer from the wire tip to the melt pool at a much lower heat energy input. Following the metal transfer, the arc is turned back on by feeding the wire back towards the weld surface. This process is repeated with a frequency (50–120 Hz) based on predefined synergic lines. It is shown that using CMT increases the controllability over the metal transfer and reduces the heat input to the part [5]. Although some variants of CMT-WAAM have improved the dimensional accuracy in printing single-track walls, the effect of CMT-WAAM process parameters on the geometry of the final parts is yet to be investigated and understood [6].

✉ G. Gary Wang
gary_wang@sfu.ca

[1] School of Mechatronic Systems Engineering, Simon Fraser University, Surrey, Canada

[2] Faculty of Engineering and Natural Sciences, Automation Technology and Mechanical Engineering, Tampere University, 33720 Tampere, Finland

Published online: 09 November 2023

As for geometry, many industries such as automotive, aerospace, and medical technologies use thin-walled features to make lightweight parts. However, most of the thin-walled parts are machined from the bulk due to the tight mechanical tolerances, which is time-consuming as a substantial volume of material that must be removed to achieve the final part's desired shape. Producing parts with near-net shape and reduced surface waviness will reduce the amount of post-process machining that is required. Hereby, producing near-net-shape thin wall structures by WAAM has been investigated by researchers. Some researchers assessed the effect of process parameters on the geometry of the single beads which includes bead width and height. Table 1 summarizes the effect of each process parameter on the bead geometry for steel. The second column of Table 1 shows primary dimensions, where L, T, M, and I represent the length, time, mass, and electrical current respectively. The correlations between process parameters and bead height and width in the WAAM process are described by positive monotonic (↑), negative monotonic (↓), and non-monotonic (NA). Studies that had different results were separated by "/." In summary and especially in the CMT-WAAM process, for low-alloy steel, the most effective parameters are the wire feed speed (WFS) and travel speed (TS) that determine the geometry and properties of the final part [7]. In fact, the dimensionless ratio of WFS to TS plays an important role in determining the geometry of the bead [8]. Nagarajan et al. [9] investigated the effect of process parameters on the geometry of the bead and found the range for the ratio of WFS to TS to be between 2.5 and 5 for mild steels to have a stable and continuous bead. As for the high-strength low-alloy (HSLA) steel, the ratio needs to be larger. Panicker et al. [10] printed single-track HSLA multi-bead walls with a WFS/TS ratio between 5 and 10.

Some researchers explore the relationships between the geometry of the thin wall structures and process parameters. For instance, Kazanas et al. [16] investigated the effect of WFS and TS on the effective wall thickness (which has a direct relationship with the bead width) and found that effective wall thickness is affected by both WFS and TS positive-monotonically and negatively monotonically, respectively. They also found that increasing the wire diameter increases the surface waviness. Yang et al. [17] found that increasing the inter-layer cooling time decreases the height variation in the thin walls; however, excessive dwell time cannot decrease the heat accumulation efficiently and will make the deposition process time-consuming. Maintaining a steady inter-pass temperature between two consecutive layers resulted in homogeneous microstructure and mechanical properties for HSLA steel walls [18].

As for modeling the part geometry with respect to process parameters, Bharat and Anandakrishnan [19] fitted a linear regression model between process parameters and bead geometries. The accuracy of the fitted models was assessed by printing single beads as confirmation tests. Moreover, Gonzalez et al. [15] found the optimal process parameters by printing single beads. Afterward, they used the optimal process parameters to print thin walls. Ma et al. [20] developed a second-order regression model that predicts the bead width and height and used their model to develop a path-planning methodology for thin walls with variable thickness. Kumar et al. [21] also developed second-order response surface models to predict the bead geometries and used the model to produce near-shape thin wall structures. Path planning strategies and part orientation are other important aspects of WAAM processes that have been investigated by researchers to achieve desired final geometries by optimizing the process parameters [22–24]. Moreover, there have been a lot of efforts to model and minimize the microscale surface roughness of metallic parts produced by DED processes [25–27]. However, studies are scarce that model and minimize the macroscale geometrical deviations of the parts. In a notable contribution by Lehmann et al. [28], a comprehensive model was developed to investigate wall width deviations, with consideration given to process parameters such as WFS and TS. Notably, this study deviated from the prevailing practice of using bead printing, instead opting for wall printing to determine optimal process parameter ranges. Ten-layered walls were printed to ascertain the most favorable conditions, with the wall width deviation (or surface waviness) serving as the response factor.

Although the wall waviness and effective wall width are established as variables to compare the quality of the width of the walls, it seems that there is not an established variable to show the quality of the height of a wall. For example, Galeazzi showed the quality of the printed walls in the CMT-WAAM process by reporting the deviation of the wall height from the mean value at different points [6]. One of the objectives of the study reported in our present work is to define a set of geometrical parameters that can characterize the height quality of a wall.

Table 1 Effect of process parameters on the bead geometry in WAAM processes made by steel (positive monotonic (↑), negative monotonic (↓), and non-monotonic (NA))

Process parameter	Unit	Bead width	Bead height	References
Wire feed speed (WFS)	LT^{-1}	↑/NA	↑	[11–13]
Travel speed (TS)	LT^{-1}	↓	↓	[11, 13, 14]
Wire diameter	L	↑	↑	[11]
Welding voltage	$ML^2T^{-3}I$	↑	↓/NA	[11, 13]
Welding current	I	↑	↑	[14, 15]
Wire stick-out*	L	↓/NA	↑/NA	[11–13]

*Distance between welding torch and top layer metal

This study aims to improve the quality of the height of the HSLA steel walls manufactured by CMT-WAAM under a fixed inter-pass temperature. As mentioned before, most of the prior work that modeled the geometry of the thin wall structures trained their models based on the single bead data whereas, in reality, the geometry of a wall is not just related to the geometry of the beads. In other words, the training data to model the geometry of the thin wall structures should be obtained from printed walls. Hence, the objectives of this study are defined as below:

- Defining a set of geometrical parameters that specifies the quality of the height of any thin wall (height-related geometrical parameters (HGPs)).
- Studying process parameters with printed thin walls based on a design of experiment (DOE) approach.
- Developing different models to predict the HGPs of thin walls and comparing them.
- Multi-objective optimization of geometrical parameters and printing the optimal thin walls for validation.
- Comparing the HGPs of thin walls printed unidirectionally and bidirectionally.

The remainder of the paper is organized as follows. Section 2 explains the methods and materials used in this research. Section 3 presents the results of the experiments and models. The results are further discussed in Section. 4 and, finally, the conclusions are drawn in Section. 5.

2 Materials and methods

The purpose is to model and optimize the quality of the height of single-track walls manufactured by metal AM processes. To achieve this, HGPs are defined and 15 walls are printed using the central composite design of experiments (DOE). The HGPs are then calculated by scanning the printed walls, modeled using different modeling approaches, and optimized to find the optimal process parameters. The optimization results are, then, validated by performing additional experiments. In the following subsections, the experimental setup, choice and range of process parameters, definition of HGPs, employed modeling approach, and the multi-objective optimization method are described in detail.

2.1 Material and experimental setup

For the CMT-WAAM experimental work, the AM70 alloy steel wire feedstock (1.2 mm diameter) is used; its chemical composition is presented in Table 2. An S355 mild steel plate ($300 \times 200 \times 20$ mm) is used as a substrate for the fabrication of a thin wall. The CMT-WAAM setup (Fig. 1) consists of a welding unit (Fronius CMT Advanced 4000) with an attached wire feeder system, a 6-axis industrial robot with a 2-axis worktable (ABB 4600 40/2.55), and an inert gas supply. The welding torch is mounted on the industrial robot arm such that the travel direction is in the X axis, the build direction is in the Z axis, and the traverse direction is in the Y axis. The computer-aided design file of the printing geometry is generated in SOLIDWORKS and imported to

Table 2 AM70 wire feedstock chemical composition [29]

Element	C	Mn	Si	Cr	Mo	Ni	Fe
Percentage (wt. %)	0.08%	1.70%	0.60%	0.20%	0.5%	1.50%	95.42%

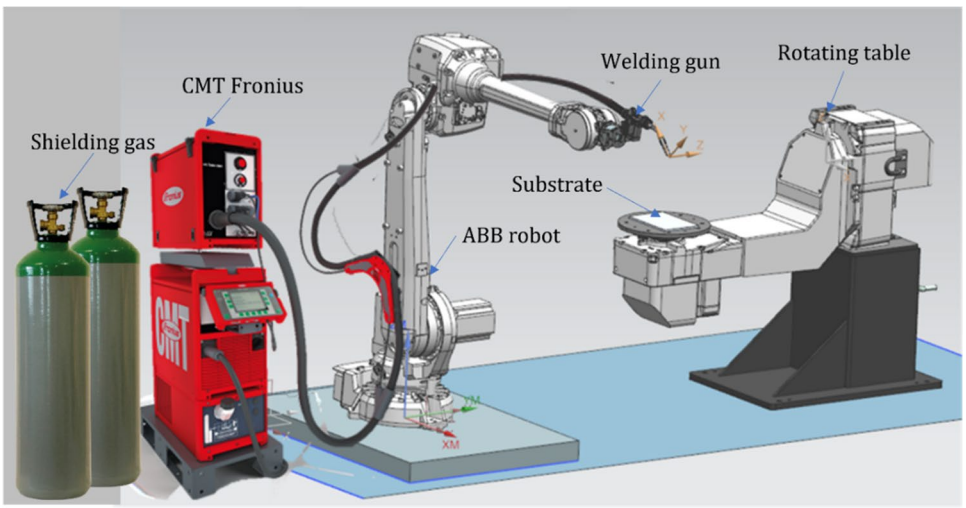

Fig. 1 CMT-WAAM equipment setup

the robot path programming software, Robot Studio 6. A contact-type digital thermal probe (Fluke 53 IIB) is used to monitor the inter-pass temperature between consecutive weld passes to be between 150 and 200 °C.

2.2 Process parameter selection and DOE

Process parameters, assumed to have the most significant effects on the final geometry of the part, are selected to be modeled in this study. TS and WFS are selected as they are the most effective parameters in the CMT-WAAM process [7]. Moreover, as shielding gas flow affects the convection heat transfer during the wall printing, it is hypothesized that it affects the quality of the height of the wall. Hence, the shielding gas flow rate (SGFR) is selected as the third process parameter. The purpose of performing experiments is to find the mathematical models between the inputs (process parameters) and outputs (HGPs). Since the model may not be linear, three levels are selected for each process parameter. The range for TS and WFS is selected in a way that the WFS/TS ratio varies from 3.33 to 12.5 as this range includes the range used by Panicker et al. [10] for low-alloy steels. Moreover, the range of SGFR is chosen to include SGFR values used by other studies done by CMT-WAAM [30–32]. Selected process parameters, levels, and their corresponding ranges are shown in Table 3. In the CMT-WAAM process, the wire is continuously retracted and pushed at a high frequency (50–120 Hz). Consequently, the WFS value is not a static, fixed value. However, for this study, we focused on a specific aspect. Specifically, we utilized the WFS value set by the operator prior to the deposition process for the modeling and optimization.

Full factorial DOE yields 27 (3^3) experiments to be performed, which is time-consuming and not cost-efficient. However, the central composite face DOE, invented by Box and Wilson [33], is commonly used as one of the robust DOE approaches to capture the significance of the impact of input parameters on the objectives as well as fitting regression models on the objectives [34–36]. Therefore, the central composite face DOE is used with 15 experiments for three levels and three factors. Table 4 shows all 15 experiments and the corresponding level of each of the process parameters.

Table 3 The range for process parameters and value for each level

Process parameter	Factor	Range	Level 1 (−1)	Level 2 (0)	Level 3 (1)
TS (mm/s)	A	8–15	8	11	15
WFS (m/min)	B	3–6	3	4.5	6
SGFR (L/min)	C	12–20	12	16	20

Table 4 Central composite face DOE for three factors and three levels

Exp. number	Factor A	Factor B	Factor C
1	−1	−1	−1
2	−1	1	1
3	−1	1	−1
4	−1	−1	1
5	1	−1	1
6	1	−1	−1
7	1	1	−1
8	1	1	1
9	0	0	0
10	−1	0	0
11	1	0	0
12	0	−1	0
13	0	1	0
14	0	0	−1
15	0	0	1

For each set of process parameters, first, a three-layer wall is printed to check if the corresponding set of process parameters would lead to a valid geometry. Then, a single-track multi-layer wall is printed for each DOE point with a length of 160 mm. All of the walls are printed unidirectionally in this stage of the experiments. Unidirectional printing and bidirectional printing are the two wall scanning strategies that are defined in Fig. 2.

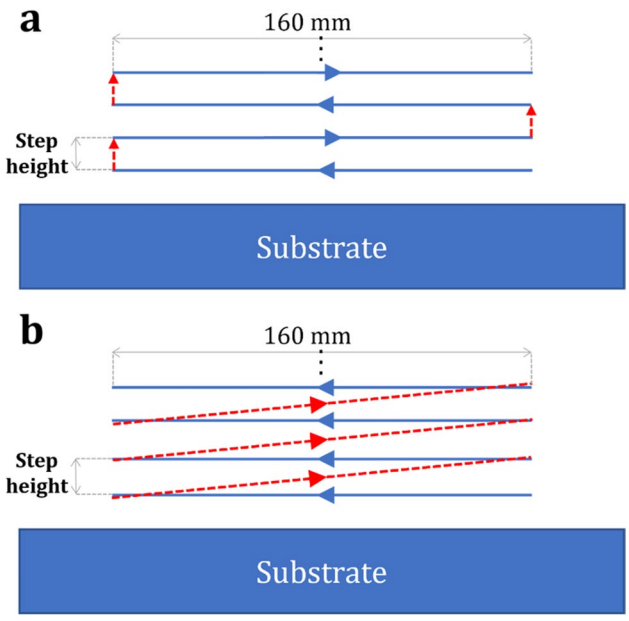

Fig. 2 **a** Bidirectional and **b** unidirectional printing directions

2.3 Pilot experiments

To understand the feasibility of the selected set of process parameters, 15 three-layer walls (one for each DOE point) are printed and the height and width of the walls are measured with a caliper (least count = 0.05 mm) from three different locations (every 40 mm after the beginning of the bead). The visual appearance of the walls is checked to ensure the feasibility of the printing of selected DOE points.

Another purpose of pilot experiments is to find the appropriate step height for the next set of experiments. It is crucial to understand the distinction between step height and layer height. The step height is a predetermined parameter, while the layer height is the actual height of each layer determined during the deposition process. If the step height is larger than the layer height, after printing a few layers, the wire stick-out increases, which leads to the wire oscillation and consequently having more spatters [37]. Conversely, if the step height is smaller than the layer height, the actual height of the wall will be more than expected after a few prints. As a result, the wire sticks to the top of the wall before the printing, and the arc will not start. Therefore, it is important to choose the step height as close as possible to the average layer height. To achieve this, the average height of the walls in the pilot experiments is chosen as the step height of the robot for the actual wall printing process.

2.4 HGP definition and geometry scanning

As mentioned earlier, a set of geometrical parameters that can specify the quality of the height of the wall is not established yet. The objective of this section is to define a set of parameters that characterize the quality of the height of thin walls. This set of parameters is called height-related geometrical parameters, HGPs. Application of HGPs is not limited to thin walls manufactured by CMT-WAAM and one can utilize HGPs to characterize, compare, and improve the quality of the height of walls manufactured by other metal additive manufacturing techniques.

First, the average height of a wall should be as close as possible to the preset height. Hence, the first parameter of the HGP is the average height error (AHE). AHE is defined as the absolute difference between the average height of the wall per layer and the step height. AHE can be represented in percentages to get a better understanding of the value of the error. Mathematically, AHE can be represented as:

$$\mathrm{AHE} = \left| \frac{\frac{H_{\mathrm{Ave}}}{n} - \mathrm{SH}}{\mathrm{SH}} \right| \tag{1}$$

where H_{Ave} is the average height of the wall over its length, n is the number of layers, and SH is the step height preset to print each wall.

The second height-related feature of a desired wall is the difference between the maximum and minimum heights of the wall, which should be kept minimum. Hence, the second parameter of HGPs is the maximum height variation (MHV). MHV can be written as:

$$\mathrm{MHV} = \left| \frac{H_{\max} - H_{\min}}{n} \right| \tag{2}$$

where $H_{\max}$ is the maximum height of the wall and $H_{\min}$ is the minimum height of the wall. To reduce the effect of the number of layers, the difference is divided by n.

Finally, the third characteristic of a flat wall is that it should have the lowest average slope throughout its length. Therefore, the last parameter of HGPs is the average absolute slope (AAS) of the wall. AAS can be formulated as:

$$\mathrm{AAS} = \frac{\mathrm{mean}\left(\left| \frac{\delta z}{\delta x} \right| \right)}{n} \tag{3}$$

where x and z axes align with travel and build directions, respectively, as shown in Fig. 3. The term $\frac{\delta z}{\delta x}$ is the slope of the wall at each point along the x axis on the top layer and mean$(\cdot)$ outputs the mean value of the slopes. A set of HGPs is a vector that describes the quality of the height of a wall. Equation 4 defines a set of HGPs for any wall. The lower is each one of the parameters, the better is the quality of the wall height. In other words, the wall with the perfect height can be described as a zero vector (HGPs = $(0, 0, 0)$).

$$\mathrm{HGPs} = (\mathrm{AHE}, \mathrm{MHV}, \mathrm{AAS}) \tag{4}$$

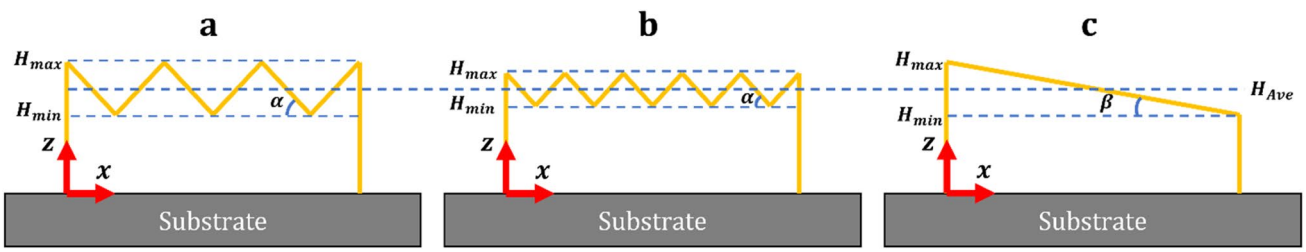

Fig. 3 Schematic of thin walls with different height variations and HGP values

The ability of the HGPs to quantify and capture the quality of the height of thin walls can be further explored by looking at Fig. 3. Figures 3(a), 3(b), and 3(c) show three walls with different height qualities that can be captured by HGPs. Since all of the walls have the same average height (same H_{Ave} dashed line), they have the same AHE value. However, the AAS value of the wall in Fig. 3(c) is lower than those in Fig. 3(a) and (b) ($\beta < \alpha$). On the other hand, the wall in Fig. 3(b) has a lower MHV value than those in Fig. 3(a) and (c). This can be understood by comparing the ($H_{\max} - H_{\min}$) values of different walls. One can understand and compare the behavior of heights of different walls by taking a look at the HGP vector of the walls. It is important to highlight that in this work HGPs are applied to thin wall structures made by single-track printing. However, the application of HGPs is not limited to single-track structures. One can use HGPs to quantify and compare the quality of height of multiple track structures as long as the thickness of the structure is negligible compared to other dimensions.

After performing the experiments, each one of the walls is scanned using a Hexagon Metrology laser scanner (HP-L-20.8 7520SE) with a scanning accuracy of 53 microns [38]. The scanned points are detected by PolyWorks 2017, and the cloud point file is saved as a ".stl" file and imported to SOLIDWORKS. The height of the wall at each point is obtained by fitting a spline to the top of the wall. The beginning and end of the wall (beginning and end of the spline) are selected at points at which the slope of the wall is greater than a large number (e.g., 100) ($\left|\frac{\delta z}{\delta x}\right| > 100$) to avoid possible ambiguity caused by edge defect. The equally spaced points of the spline are output to a MATLAB script where the HGPs are determined for each wall.

2.5 Statistical analysis, modeling, and optimization

After scanning the walls and preparing responses (HGPs) for all of the walls, a single variate analysis of variances (ANOVA) is performed to understand the significance of process parameters on HGPs of the wall. From the result of ANOVA, the responses (HGPs) that are affected significantly by process parameters are modeled. K-fold cross-validation is used as only limited data is available. Four different metamodeling approaches including Gaussian process regression (GPR), kriging (KRG), Gaussian radial basis function (GRBF), and second-order response surface model (RSM) are used. The difference between GPR and KRG is that GPR has a random noise added to the base KRG model. The metamodeling approach that leads to the highest R-squared (R^2) value is selected as the final model.

The process parameters that lead to the lowest HGPs are selected by optimizing the modeled HGPs using multi-objective optimization (MOO). MOO is performed using the OASIS software tool and one point is selected from the Pareto frontier as the optimal point. OASIS is an optimization software tool that is designed to solve low- to high-dimensional single-/multi-objective optimization problems [39]. The optimal set of process parameters is used to print two walls to verify the quality improvement and the model's accuracy.

2.6 Comparing unidirectional and bidirectional printing

Using the optimal process parameters found in the previous step, a single-track multi-layer wall is printed with the bidirectional printing strategy. The HGPs of the wall are compared with the wall printed unidirectionally.

3 Results

3.1 Pilot experiments

A three-layer single-track wall is printed for each set of process parameters. The visual appearance of some of the DOE points is shown in Fig. 4. From the visual appearance of the beads, it is concluded that all the DOE points lead to feasible prints, and the process is stable for all cases. Moreover, the average layer height, width, and WFS/TS ratio for each experiment are shown in Table 5. The step height for the experiments described in Sect. 3.2 is specified as the average layer height of the pilot experiments. It is also worth noting that the WFS/TS ratio is highly correlated with the layer height and width, as shown in Table 5. The relationship between WFS/TS and wire and bead cross-sectional areas

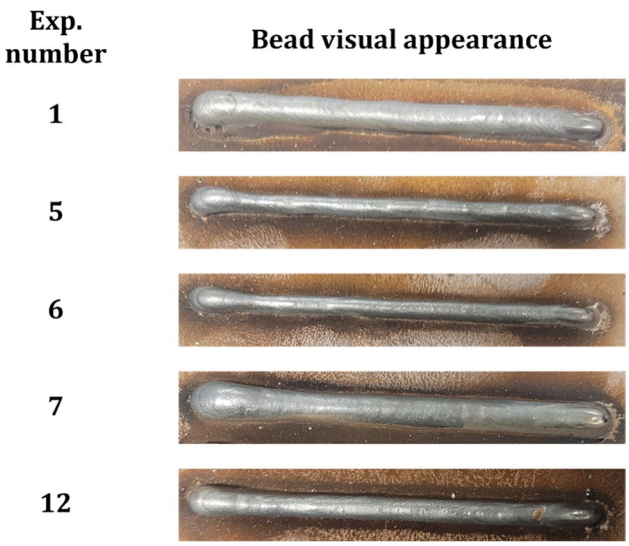

Fig. 4 Bead visual appearance of beads printed with some of the DOE points in the pilot experiments

Table 5 The average layer height for each of the DOE points (calculated from three-layer beads)

Exp. number	Average layer height (mm)	Average layer width (mm)	WFS/TS ratio
1	1.90	5.77	6.25
2	1.82	8.55	12.5
3	1.89	8.77	12.5
4	1.70	5.40	6.25
5	1.34	4.13	3.33
6	1.30	4.03	3.33
7	1.59	6.70	6.67
8	1.43	6.70	6.67
9	1.64	5.52	6.82
10	1.79	7.27	9.38
11	1.87	6.88	5.00
12	1.36	4.65	4.55
13	1.69	7.97	9.09
14	1.62	7.03	6.82
15	1.75	6.13	6.82

can be explained by Eqs. 5 and 6. Using the conservation of mass, it can be concluded that:

$$\mathrm{WFS} \times A_{\mathrm{wire}} = \mathrm{TS} \times A_{\mathrm{bead}} \tag{5}$$

where A_{bead} and A_{wire} are the bead and wire cross-sectional areas, respectively. By dividing two sides of Eq. 5 by $\mathrm{TS} \times A_{\mathrm{wire}}$, it is derived that:

$$\frac{\mathrm{WFS}}{\mathrm{TS}} = \frac{A_{\mathrm{bead}}}{A_{\mathrm{wire}}} \tag{6}$$

where the WFS/TS ratio is equal to the ratio of the cross-sectional area of the printed bead to the wire cross-sectional area. As the wire cross-section is constant during the process, the higher the WFS/TS ratio, the higher the printed bead cross-sectional area, which is the double integral of the layer height and width.

3.2 Printing multi-layer thin walls and performing ANOVA

After printing the multi-layer thin walls, three of the walls (DOE points 5, 6, and 12) are rejected as they have sawtooth waves on the surface, and calculating the HGPs is neither feasible nor reasonable for these DOE points. The sawtooth waves can be seen for DOE points 6 and 12 in Fig. 5. Although the appearance and geometry of the three-layer wall with the same process parameters are checked and approved in the pilot experiment, the final geometry after the print is not desirable.

HGP vectors for all the 12 remaining DOE points are calculated and ANOVA is performed for each of the responses including the average height error (AHE), maximum height variation (MHV), and average absolute slope (AAS). Table 6 summarizes the ANOVA results for AHE, MHV, and AAS. It can be seen that the most significant impacts are (1) the effect of wire feed speed on the maximum height variation (P-value = 0.041) and (2) the effect of travel speed on the

Table 6 Summary of the ANOVA for all three responses (AHE, MHV, and AAS)

Process parameter	P-value		
	AHE	MHV	AAS
Travel speed (TS)	0.1971	0.1357	0.0865
Wire feed speed (WFS)	0.9297	0.041	0.3717
Shielding gas flow rate (SGFR)	0.2834	0.5583	0.4067

Fig. 5 Sawtooth waves of the multi-layer walls printed with DOE points 6 (top) and 12 (bottom)

average absolute slope (P-value = 0.0865). Based on the P-values presented in Table 6, it can be concluded that the WFS and TS are the most significant factors for MHV and AAS, respectively. On the other hand, none of the parameters seems to have a significant effect on AHE.

3.3 Modeling of height-related geometrical parameters

To further investigate the effect of process parameters on MHV and AAS, these two parameters are modeled with different metamodeling approaches. The relationship between the process parameters and AHE is not modeled as it seems that none of the selected process parameters has a significant impact on AHE. As the number of DOE points is limited (12 data points), fourfold cross-validation is used. In fourfold cross-validation, four metamodels are developed and the final predicted value is the average value of all four models. The first metamodel is trained using data points 4 to 12 (9 points). The second one is trained using data points 1–3 and 7–12 (9 points in total), and so on. The final model is the average value of these four models. Tables 7 and 8 show different prediction and experimental values of all 12 experiments for AAS and MHV, respectively. The last row compares the R-squared value calculated on all of the data points for different metamodels. In Table 7, the GRBF model leads

Table 7 Experimental and model values of AAS of walls printed with different DOE points

Exp. number	Process parameters			AAS model predictions				Experimental AAS value
	TS (mm/s)	WFS (m/min)	SGFR (L/s)	GPR	**GRBF***	KRG	RSM	
1	8	3	12	0.2905	**0.2801**	0.2956	0.2819	0.2727
2	8	6	20	0.2327	**0.2304**	0.2379	0.2488	0.2297
3	8	6	12	0.2009	**0.2053**	0.2075	0.2036	0.1878
4	8	3	20	0.2200	**0.2202**	0.2243	0.2926	0.2128
7	15	6	12	0.2970	**0.3109**	0.3050	0.3690	0.3159
8	15	6	20	0.2536	**0.2657**	0.2614	0.2516	0.2581
9	11	4.5	16	0.2747	**0.2681**	0.2655	0.2719	0.2612
10	8	4.5	16	0.2327	**0.2346**	0.2332	0.2505	0.2301
11	15	4.5	16	0.2855	**0.3024**	0.2957	0.2998	0.3007
13	11	6	16	0.2844	**0.2675**	0.2675	0.2859	0.2755
14	11	4.5	12	0.2699	**0.2802**	0.2774	0.2693	0.2796
15	11	4.5	20	0.2536	**0.2532**	0.2535	0.2276	0.2579
R-squared value				0.9111	**0.9499**	0.9413	0.2818	

*The bold column shows the selected model

Table 8 Experimental and model values of MHV of walls printed with different DOE points

Exp. number	Process parameters			MHV model prediction				Experimental MHV value (mm)
	TS (mm/s)	WFS (m/min)	SGFR (L/s)	GPR	GRBF	**KRG***	RSM	
1	8	3	12	0.6364	0.7771	**0.6887**	0.8851	0.6551
2	8	6	20	1.2486	1.2106	**1.2711**	1.0311	1.1265
3	8	6	12	1.1520	1.2543	**1.2016**	1.2403	1.2347
4	8	3	20	0.7322	0.7965	**0.7745**	0.6522	0.8367
7	15	6	12	0.8716	0.9806	**0.9274**	0.7122	0.8955
8	15	6	20	0.8712	0.8418	**0.9129**	0.8562	0.8949
9	11	4.5	16	1.0438	0.9692	**1.0249**	0.9904	1.0235
10	8	4.5	16	0.9198	0.9485	**0.9849**	0.8292	0.9514
11	15	4.5	16	0.8965	0.8625	**0.9346**	1.0705	0.9286
13	11	6	16	0.9915	1.0663	**1.0433**	0.9242	1.0564
14	11	4.5	12	1.0183	1.0696	**1.0886**	1.1798	1.1251
15	11	4.5	20	0.7865	0.8388	**0.8567**	1.0703	0.7809
R-squared value				0.8768	0.8404	**0.8900**	0.2943	

*The bold column shows the selected model

to the highest R-squared value ($R^2 = 0.9499$); hence, GRBF is chosen as the model to predict AAS, the average absolute change of the height per unit length per layer of the wall. By comparing the experimental AAS values (last column) under different process parameters, it can be understood that the AAS and TS have a positive monotonic relationship. This means that increasing the travel speed leads to more variation in the slope of the thin walls.

For MHV, as shown in Table 8, KRG outperforms other metamodeling approaches and is selected to be exploited in further analyses ($R^2 = 0.8900$). It is worth mentioning that MHV values in Table 8 represent the difference between the highest and lowest points of the wall per layer. It can be understood from the experimental data in Table 8 that the WFS and MHV have a positive monotonic relationship. In other words, lower WFS leads to lower height difference.

3.4 Multi-objective optimization and confirmation tests

To find the optimal process parameters that lead to the lowest AAS and MHV values, MOO is used. The multi-objective optimization is formulated using Eq. 7.

$$\min \ (\mathrm{AAS}(x), \ \mathrm{MHV}(x)) \tag{7}$$

Subject to:

$$x_{\min} \leq x \leq x_{\max}$$

where x is the vector of process parameters containing TS, WFS, and SGFR as the design variables. AAS(x) and MHV(x) are the mathematical models of average absolute slope and maximum height variations, respectively, developed in the previous step. $x_{\min}$ and $x_{\max}$ are the bounds of the design space that can be found in Table 3 for each design variable (process parameter).

After performing MOO and analyzing the Pareto frontier, it is found that all of the optimal points have the same TS and WFS at their lowest level (TS = 8 mm/s, WFS = 3 m/min) with variations only in SGFR. MHV and AAS values of different Pareto frontier points can be seen in Fig. 6. The red square point is selected as the optimal point. The process parameters of the selected point are TS = 8 mm/s, WFS = 3 m/min, and SGFR = 17 L/min. The reason to choose this point is to have a compromise between both objectives (MHV and AAS). This compromise is explained more in Sect. 4.3.

To check the accuracy of the models and find process variations, two multi-layer single-track walls are printed using the optimal process parameters. The geometry of both printed walls can be seen in Fig. 7(a) and (b). Visually, the geometries of the walls are similar and both of them suffer from edge defect which is a result of unidirectional printing

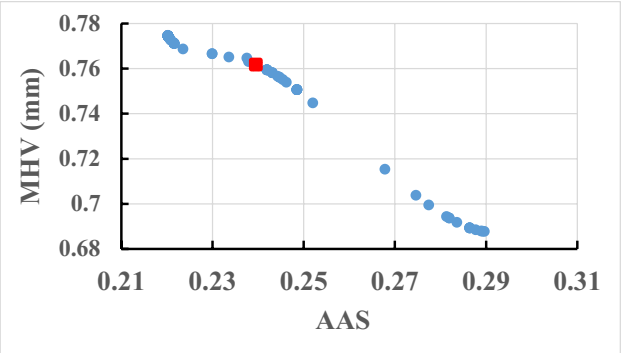

Fig. 6 Pareto frontier of multi-objective optimization of MHV and AAS

[40]. HGPs of both walls can be compared in the first two rows of Table 9. The reason for printing two walls with the same process parameters is to investigate the repeatability of the process and the effect of uncertainties on the final geometry of the wall. The repeatability of the process can be understood by comparing the visual appearance of the printed walls. It can be further validated by analyzing the differences in the HGP values. The differences between the HGP values of the two walls are 6.3%, 4.5%, and 2.2% for AHE, MHV, and AAS, respectively, which shows that HGPs of the printed walls are very close to each other and the process is repeatable.

The prediction values for MHV and AAS can be seen in the third row of Table 9. To check the validity of the developed models, one method is to find the confidence interval from the experiments and test if the estimated value lies in the confidence interval. The experimental confidence interval is the experimental mean ± experimental standard deviation. This experimental confidence interval is equal to the interval between the experimental data points if the number of experiments is two. Hence, the developed models for each one of the responses are valid, if the estimated value is between the two experimental values. As for the MHV, the predicted value (MHV = 0.7618) is in the interval [0.7309, 0.7638]; hence, the maximum height variation model is valid. However, the AAS model is not validated as the AAS predicted value (AAS = 0.2395) is out of the confidence interval, which will be discussed in Sect. 4.2.

3.5 Unidirectional vs. bidirectional

One of the factors that can reduce the edge defect in thin walls is the scanning strategy. Printing the walls bidirectionally would decrease the edge defect as described in the literature [9, 40]. Hence, one multi-layer single-track wall is printed bidirectionally. From the visual appearance, it is found that the geometry is improved as shown in Fig. 7(c), compared with the walls printed unidirectionally. In terms

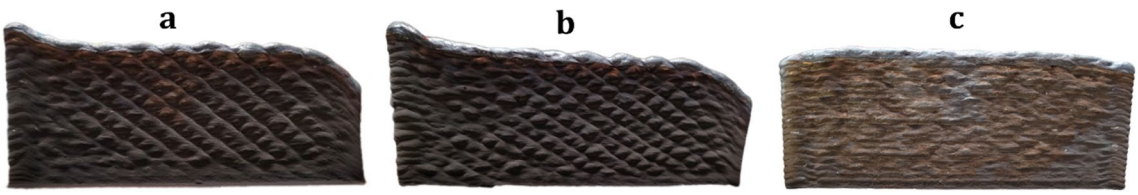

Fig. 7 Side view of the walls printed with optimal process parameters. **a** and **b** were printed unidirectionally and **c** was printed bidirectionally

of quantitative parameters, the improvement can be seen by comparing the HGP values of unidirectional and bidirectional prints in Table 9. The values of AHE and MHV are significantly reduced when the part is printed bidirectionally. The amount of decrease in the AAS value, however, is not as significant as the other two HGPs (AHE and MHV).

4 Discussion

4.1 Process stability and WFS/TS ratio

To check if the process is stable for all of the DOE points, three-layer walls are printed. All of the beads are continuous, and the process seems to be stable. However, in some of the real experiments (DOE points 5, 6, and 12) and after printing 5–10 layers, the process becomes unstable, and a sawtooth wave pattern appears and grows layer by layer. This observation confirms our hypothesis that to optimize the WAAM process parameters, the models should not be trained on data gathered from bead printings as the final geometry is determined after printing 5–10 layers. Moreover, by checking the average layer height of DOE points 5, 6, and 12 in Table 5, one can understand that these three DOE points have the least average layer height (all below 1.4 mm). Therefore, if one wants to check the stability of the print, the average layer height of the beads should be checked rather than checking the visual appearance of the beads. Our observation shows that for any specific machine and material, there is a layer height threshold that if the process parameters lead to a lower layer height than the threshold, it will print an unstable wall. This threshold is found to be 1.4 mm for the used machine and material (AM70) in this paper since any wall that has an average layer height less than 1.4 mm (based on Table 5) is printed with instability (DOE points 5, 6, and 12). This can also be found by checking the wire feed speed to travel speed ratio since the cross-section of the bead is the result of the multiplication of this ratio with the wire cross-sectional area (last column of Table 5). Based on the experimental results, we find that the WFS/TS threshold is around 4.9 as the ratio for the failed experiments (DOE points 5, 6, and 12) is below 4.9.

Table 9 Height-related geometrical parameters of the printed walls with optimal process parameters

	AHE	MHV (mm)	AAS
Unidirectional printing 1	0.0358	0.7638	0.2715
Unidirectional printing 2	0.0382	0.7309	0.2654
Models' predictions	-	0.7618	0.2395
Bidirectional printing	0.0144	0.1866	0.2431

4.2 Model validity and future considerations to improve height quality

The results of confirmation tests show that the model to predict MHV is valid. However, the AAS model is not validated as the AAS predicted value is not in the confidence interval found from the confirmation tests. One way to validate the AAS model is to train the model with more experiments and apply the calibration framework defined in ref. [41] where a bias between the predicted model and experimental values is defined and calibrated in a loop. Although the later model is not valid, the aforementioned relationships between process parameters and AAS still exist. For example, it is found that the travel speed has the most significant impact on the AAS value (Table 6) and the relationship between AAS and TS is positive monotonic. It means that by increasing the travel speed, the height of the wall will have more variations. The *P*-values for AHE are all above 0.197 and thus this parameter cannot be controlled by the process parameters defined in this study. Hence, AHE is not modeled as a function of process parameters. The effect of other parameters such as wire stick out, interpass temperature, arc current and voltage on AHE should be further investigated in future studies.

4.3 ANOVA and optimization results

The result of ANOVA test shows that AAS and MHV are mostly controlled by TS and WFS, respectively (Table 6). Moreover, the results represented on Tables 7 and 8 show that TS and WFS have positive monotonic relationships with AAS and MHV, respectively. These results are aligned with the optimal points on Pareto frontier, as all the optimal points have the same TS and WFS values. The selected optimal point for validation tests is chosen in a way that can be explained by Fig. 8. Figure 8 shows the MHV and AAS

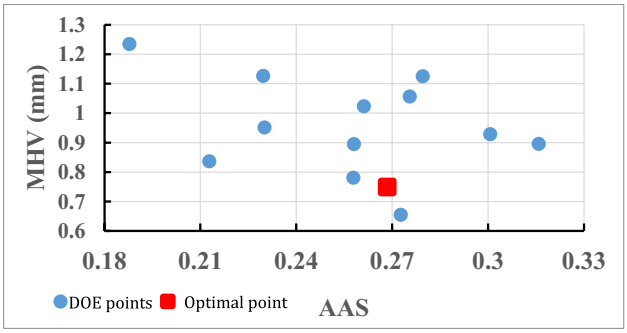

Fig. 8 MHV and AAS values of DOE points (blue round points) and optimal unidirectionally printed wall (square red point)

values of the DOE experimental points (12 data points) as well as the average values of MHV and AAS from two optimally printed walls (red square point). The optimal wall has a lower MHV value than 11 out of the 12 walls. Similarly, the optimal wall has lower AAS value than 5 out of the 12 walls.

4.4 Comparison of printing strategies and HGP capabilities

By comparing the visual appearance of unidirectionally printed walls (Fig. 7(a) and (b)) and the bidirectionally printed wall, it can be understood that the bidirectional printing leads to less height variation and a more even wall surface. This can be confirmed by comparing HGP values shown in Table 9. The AHE and MHV values of the bidirectionally printed wall are significantly lower than those of the unidirectionally printed walls, respectively. It confirms the hypothesis that the printing strategy can improve the quality of the height of the wall and prevents edge defect in the walls [40, 42]. Moreover, it shows that the height-related geometrical parameters defined in this study are able to represent the quality of the height of the wall. By comparing the AAS value of the walls printed with different printing strategies (the last column of Table 9), it can be understood that although bidirectional printing leads to less AAS value ($0.2431 < 0.2654$), the difference is not as significant as the difference in the other two HGPs (MHV and AHE). The reason is that AAS captures how sharp the height changes and how many times the slope sign changes. Although the quality of the height of the wall improves by printing bidirectionally, there are some small waves on the top surface of the bidirectionally printed wall (Fig. 7c) that are captured by AAS. As a result, the value of the AAS does not drop significantly compared to the walls printed unidirectionally. The small waves on the top surface of the bidirectionally printed wall could be missed if the HGP values do not include AAS.

4.5 Model generalization and future studies

It is worth mentioning that if the developed models are intended to be applied to other alloys or geometries, it is essential to verify the generalization of the models by conducting similar experiments on different materials and geometries. Future studies should focus on checking the generalization of the developed models. However, the height-related geometrical parameters defined in this study offer broader applicability, as they can be utilized to assess the height quality of thin structures produced using metal additive manufacturing technologies, regardless of the specific alloy, geometry, or process.

In Fig. 7, it can be noticed that although the quality of the height of the walls improves by optimizing height-related geometrical parameters, there are some bumps in an inclined pattern and the quality of the width of the walls still needs to be improved. This can be a future investigation where both the width and height of the single-track multi-layer walls could be modeled and optimized. Moreover, the process parameters are optimized to improve the quality of the height of the single-track straight walls. The optimized process parameters would differ if other geometries are printed (e.g., cylinders, tilted walls). In future studies, the same method will be applied to optimize the process parameters for different geometries and be generalized for parts with complex geometries.

5 Conclusion

A set of height-related geometrical parameters (HGPs) is defined to represent the quality of the height of single-track walls printed by CMT-WAAM. The central composite faced DOE is used to print 15 single-track walls with three variable process parameters, namely, travel speed (TS), wire feed speed (WFS), and shielding gas flow rate (SGFR). It is found that the stability of the print cannot be guaranteed by printing single beads and a wall of at least 5–10 layers should be printed to check if the selected parameters lead to stable prints. A minimum threshold of 4.9 for the WFS/TS ratio is introduced for AM70 to print single-track stable walls by CMT-WAAM. The HGPs of printed walls are modeled and it is found that TS and WFS significantly affect the average absolute slope (AAS) and maximum height variation (MHV) of the walls, respectively. Since none of the process parameters has a significant impact on the average height error (AHE), this HGP is neither modeled nor optimized. The quality of the height of the wall is optimized by performing MOO, and a validation test is performed to validate the models. It is found that the MHV model is valid, but more experiments should be performed to validate the AAS model. With the same process parameters, a single-track

wall is printed bidirectionally to be compared with the walls printed unidirectionally. Defined HGPs are not only able to quantify the differences in visual appearance of the height of the walls but they could capture the quality of the height of the wall with only three parameters. The future work would be to apply the calibration and validation framework defined in ref. [41] to validate the AAS model and also calibrate the uncertainties in the process. Moreover, another future work is to model and optimize the width and height of the wall simultaneously.

Author contribution All authors contributed to performing and completing this research study. Specifically, the definition of the height-related geometrical parameters and designing and performing the experiments (partially) were performed by MRD, SP, and YT. The data collection is performed by DW. GGW and EC contributed to the development of the height-related geometrical parameters, modeling, and optimization of the parameters. The first draft of the manuscript was written by MRD and all authors commented on previous versions of the manuscript. All authors read and approved the final manuscript.

Funding The authors gratefully acknowledge funding from the Natural Sciences and Engineering Research Council (NSERC) of Canada (grant numbers: RGPIN-2019–06601) and Business Finland under Project #: 4819/31/2021 with affiliation to the Eureka! SMART project (S0410) titled "TANDEM: Tools for Adaptive and Intelligent Control of Discrete Manufacturing Processes."

Declarations

Competing interests The authors declare no competing interests.

References

1. Baufeld B, der Biest O, Van GR (2010) Additive manufacturing of Ti–6Al–4V components by shaped metal deposition: microstructure and mechanical properties. Mater Des 31:S106–S111. https://doi.org/10.1016/j.matdes.2009.11.032
2. Ngo TD, Kashani A, Imbalzano G et al (2018) Additive manufacturing (3D printing): a review of materials, methods, applications and challenges. Compos Part B Eng 143:172–196. https://doi.org/10.1016/j.compositesb.2018.02.012
3. Pickin CG, Young K (2006) Evaluation of cold metal transfer (CMT) process for welding aluminum alloy. Sci Technol Weld Join 11:583–585. https://doi.org/10.1179/174329306X120886
4. Feng J, Zhang H, He P (2009) The CMT short-circuiting metal transfer process and its use in thin aluminum sheets welding. Mater Des 30:1850–1852. https://doi.org/10.1016/j.matdes.2008.07.015
5. Zhang HT, Feng JC, He P et al (2009) The arc characteristics and metal transfer behaviour of cold metal transfer and its use in joining aluminum to zinc-coated steel. Mater Sci Eng A 499:111–113. https://doi.org/10.1016/j.msea.2007.11.124
6. Galeazzi D, Silva RH, Viviani AB et al (2022) Evaluation of thermal and geometric properties of martensitic stainless steel thin walls built by additive manufacturing cold metal transfer (CMT) processes. Int J Adv Manuf Technol 120:2151–2165. https://doi.org/10.1007/s00170-022-08921-x
7. Yildiz AS, Davut K, Koc B, Yilmaz O (2020) Wire arc additive manufacturing of high-strength low alloy steels: study of process parameters and their influence on the bead geometry and mechanical characteristics. Int J Adv Manuf Technol 108:3391–3404. https://doi.org/10.1007/s00170-020-05482-9
8. Näkki J (2018) Properties of alloy 625 claddings made with laser and CMT methods. Doctoral thesis, Tampere University of Technology, Tampere, Finland
9. Nagarajan HPN, Panicker S, Mokhtarian H et al (2019) Graph-based metamodeling for characterizing cold metal transfer process performance. Smart Sustain Manuf Syst 3:169–189. https://doi.org/10.1520/SSMS20190026
10. Panicker S, Nagarajan HPN, Tuominen J et al (2022) Investigation of thermal influence on weld microstructure and mechanical properties in wire and arc additive manufacturing of steels. Mater Sci Eng A 853:143690. https://doi.org/10.1016/j.msea.2022.143690
11. Dickens PM, Pridham MS, Cobb RC et al (1992) Rapid prototyping using 3-D welding. International Solid Freeform Fabrication Symposium, University of Texas at Austin, Austin, Texas, United States of America. http://hdl.handle.net/2152/64409
12. Song Y-A, Park S, Chae S-W (2005) 3D welding and milling: part II—optimization of the 3D welding process using an experimental design approach. Int J Mach Tools Manuf 45:1063–1069. https://doi.org/10.1016/j.ijmachtools.2004.11.022
13. Lu X, Zhou YF, Xing XL et al (2017) Open-source wire and arc additive manufacturing system: formability, microstructures, and mechanical properties. Int J Adv Manuf Technol 93:2145–2154. https://doi.org/10.1007/s00170-017-0636-z
14. Prado-Cerqueira JL, Diéguez JL, Camacho AM (2017) Preliminary development of a wire and arc additive manufacturing system (WAAM). Procedia Manuf 13:895–902. https://doi.org/10.1016/j.promfg.2017.09.154
15. González J, Rodríguez I, Prado-Cerqueira JL et al (2017) Additive manufacturing with GMAW welding and CMT technology. Procedia Manuf 13:840–847. https://doi.org/10.1016/j.promfg.2017.09.189
16. Kazanas P, Deherkar P, Almeida P et al (2012) Fabrication of geometrical features using wire and arc additive manufacture. Proc Inst Mech Eng Part B J Eng Manuf 226:1042–1051
17. Yang D, Wang G, Zhang G (2017) Thermal analysis for single-pass multi-layer GMAW based additive manufacturing using infrared thermography. J Mater Process Technol 244:215–224. https://doi.org/10.1016/j.jmatprotec.2017.01.024
18. Zhai W, Wu N, Zhou W (2022) Effect of interpass temperature on wire arc additive manufacturing using high-strength metal-cored wire. Metals (Basel) 12. https://doi.org/10.3390/met12020212
19. Bharat Kumar CH, Anandakrishnan V (2020) Experimental investigations on the effect of wire arc additive manufacturing process parameters on the layer geometry of Inconel 825. Mater Today Proc 21:622–627. https://doi.org/10.1016/j.matpr.2019.06.727
20. Ma G, Zhao G, Li Z, Xiao W (2019) A path planning method for robotic wire and arc additive manufacturing of thin-walled structures with varying thickness. IOP Conf Ser Mater Sci Eng 470:12018. https://doi.org/10.1088/1757-899X/470/1/012018
21. Kumar A, Maji K (2020) Selection of process parameters for near-net shape deposition in wire arc additive manufacturing by genetic algorithm. J Mater Eng Perform 29:3334–3352. https://doi.org/10.1007/s11665-020-04847-1
22. Alomari Y, Birosz MT, Andó M (2023) Part orientation optimization for wire and arc additive manufacturing process for convex and non-convex shapes. Sci Rep 13:2203. https://doi.org/10.1038/s41598-023-29272-x
23. Venturini G, Montevecchi F, Scippa A, Campatelli G (2016) Optimization of WAAM deposition patterns for T-crossing features. Procedia CIRP 55:95–100. https://doi.org/10.1016/j.procir.2016.08.043

24. Singh S, Sharma S, kumar, Rathod DW (2021) A review on process planning strategies and challenges of WAAM. Mater Today Proc 47:6564–6575. https://doi.org/10.1016/j.matpr.2021.02.632
25. Omar SMT, Plucknett KP (2023) Influence of layer thickness upon the dimensional accuracy and surface roughness of AISI D2 tool steel manufactured using directed energy deposition. In: Proceedings of the 61st Conference of Metallurgists, COM 2022. Springer, Cham. https://doi.org/10.1007/978-3-031-17425-4_7
26. Amiri M, Crawford GA, Earthman JC (2021) Quantitative percussion diagnostics for evaluating porosity and surface roughness of cold sprayed and laser deposited materials. J Mater Res Technol 14:312–323. https://doi.org/10.1016/j.jmrt.2021.06.047
27. Pereira A, Carou D, Fenollera M et al (2022) Experimental study on the manufacturing of steel inclined walls by directed energy deposition based on dimensional and 3D surface roughness measurements. Materials 15(14):4994
28. Lehmann T, Jain A, Jain Y et al (2020) Concurrent geometry- and material-based process identification and optimization for robotic CMT-based wire arc additive manufacturing. Mater Des 194:108841. https://doi.org/10.1016/j.matdes.2020.108841
29. Bohler 3D PrintAM70, low-alloyed, high-strength steel, Material Safety Data Sheet. https://www.vabw-service.com/documents/boehler/datenblaetter/en/L1_34551_en__3Dprint_AM_70_1H43C006_3367515__EN%20(1).pdf?cache=1639059520
30. Rodriguez N, Vázquez L, Huarte I et al (2018) Wire and arc additive manufacturing: a comparison between CMT and TopTIG processes applied to stainless steel. Weld World 62:1083–1096. https://doi.org/10.1007/s40194-018-0606-6
31. Rodrigues TA, Duarte V, Avila JA et al (2019) Wire and arc additive manufacturing of HSLA steel: effect of thermal cycles on microstructure and mechanical properties. Addit Manuf 27:440–450. https://doi.org/10.1016/j.addma.2019.03.029
32. Le VT, Mai DS, Doan TK, Paris H (2021) Wire and arc additive manufacturing of 308L stainless steel components: optimization of processing parameters and material properties. Eng Sci Technol an Int J 24:1015–1026. https://doi.org/10.1016/j.jestch.2021.01.009
33. Box GEP, Wilson KB (1951) On the experimental attainment of optimum conditions. J Royal Stat Soc 13:1–45. https://doi.org/10.1111/j.2517-6161.1951.tb00067.x
34. Kazmi KH, Sharma SK, Das AK et al (2023) Wire arc additive manufacturing of ER-4043 aluminum alloy: effect of tool speed on microstructure, mechanical properties and parameter optimization. J Mater Eng Perform. https://doi.org/10.1007/s11665-023-08309-2
35. Geng H, Xiong J, Huang D et al (2017) A prediction model of layer geometrical size in wire and arc additive manufacture using response surface methodology. Int J Adv Manuf Technol 93:175–186. https://doi.org/10.1007/s00170-015-8147-2
36. Durão LFCS, Barkoczy R, Zancul E et al (2019) Optimizing additive manufacturing parameters for the fused deposition modeling technology using a design of experiments. Prog Addit Manuf 4:291–313. https://doi.org/10.1007/s40964-019-00075-9
37. Kaplan AFH, Powell J (2011) Spatter in laser welding. J Laser Appl 23:32005. https://doi.org/10.2351/1.3597830
38. Hexagon Meterology (2016) HP-L-20.8 laser scanner for ROMER absolute arm. https://go.mi.hexagon.com/l/980223/2023-04-17/35vjq9?utm_source=google&utm_medium=cpc&utm_term=arm-red-tag&utm_campaign=na-us-2023-md-arm-red-tag-q3&creative=666765148964&keyword=romer%20absolute%20arm&matchtype=p&network=g&device=c&gad_source=1&gclid=CjwKCAjwkY2qBhBDEiwAoQXK5WD2FbuDN9LWXHg0owpmx1_6PYIVgY_bB22oIFp6tQIrZWedUucEvhoCHNgQAvD_BwE
39. Empower operations. https://empowerops.com/
40. Miedzinski M (2017) Materials for additive manufacturing by direct energy deposition. Master's thesis in Materials Engineering, Chalmers University of Technology, Gothenburg, Sweden. https://publications.lib.chalmers.se/records/fulltext/253822/253822.pdf
41. Rahmani Dehaghani M, Tang Y, Wang GG (2022) Iterative uncertainty calibration for modeling metal additive manufacturing processes using statistical moment-based metric. J Mech Des 145. https://doi.org/10.1115/1.4055149
42. Liu M, Kumar A, Bukkapatnam S, Kuttolamadom M (2021) A review of the anomalies in directed energy deposition (DED) processes & potential solutions - part quality & defects. Procedia Manuf 53:507–518. https://doi.org/10.1016/j.promfg.2021.06.093